1   **A GeoNEX-based high spatiotemporal resolution product of land surface downward**
2   **shortwave radiation and photosynthetically active radiation**

4   Ruohan Li [1], Dongdong Wang[1], Weile Wang [2], Ramakrishna Nemani [2],

6   [1] Department of Geographical Sciences, University of Maryland, College Park, MD 20742, USA

7   [2] NASA Ames Research Center, Mountain View, CA 94043, USA

9   *Correspondence to*: Dongdong Wang (ddwang@umd.edu)

11   **Abstract.** Surface downward shortwave radiation (DSR) and photosynthetically active radiation (PAR) play
12   critical roles in the Earth's surface processes. As the main inputs of various ecological, hydrological, carbon,
13   and solar photovoltaic models, increasing requirements for high spatiotemporal resolution DSR and PAR
14   estimation with high accuracy have been observed in recent years. However, few existing products satisfy all of
15   these requirements. This study employed a well-established physical-based look-up table (LUT) approach to the
16   GeoNEX gridded top-of-atmosphere bidirectional reflectance factor data acquired by the Advanced Himawari
17   Imager (AHI) and Advanced Baseline Imager (ABI) sensors. It produced a data product of DSR and PAR over
18   both AHI and ABI coverage at an hourly temporal step with a 1 km spatial resolution. GeoNEX DSR data were
19   validated over 63 stations, and GeoNEX PAR data were validated over 27 stations. The validation showed that
20   the new GeoNEX DSR and PAR products have accuracy higher than other existing products, with root mean
21   square error (RMSE) of hourly GeoNEX DSR achieving $74.3\ W/m^2$ (18.0%), daily DSR estimation achieving
22   $18.0\ W/m^2$ (9.2%), hourly GeoNEX PAR achieving $34.9\ W/m^2$ (19.6%), and daily PAR achieving $9.5\ W/m^2$
23   (10.5%). The study also demonstrated the application of the high spatiotemporal resolution GeoNEX DSR
24   product in investigating the spatial heterogeneity and temporal variability of surface solar radiation. The data
25   product can be accessed through NASA Advanced Supercomputing Division GeoNEX data portal
26   https://data.nas.nasa.gov/geonex/geonexdata/GOES16/GEONEX-L2/DSR-PAR/ and
27   https://data.nas.nasa.gov/geonex/geonexdata/HIMAWARI8/GEONEX-L2/DSR-PAR/
28   (https://doi.org/10.5281/zenodo.7023863, Wang & Li, 2022).

29   **1.   Introduction**

30   Surface downward shortwave radiation is of great importance to the surface energy balance and hence is the
31   required input of various surface models. Downward shortwave radiation (DSR) is defined as solar radiation
32   received at the Earth's surface within the wavelength range of 300–4000 nm. It is the fundamental driving force
33   of many global ecological, hydrological, and biochemical processes (Huang et al., 2019; Wang et al., 2021;
34   Liang et al., 2019) and provides one of the most promising renewable energy sources, solar energy.
35   Photosynthetically active radiation (PAR) is the visible component of DSR in the spectral range of 400–700 nm.
36   It also serves as the main input for terrestrial ecosystem modeling, carbon cycle modeling, and yield estimations
37   because of its functionality in photosynthesis (Prince and Goward, 1995; Gu et al., 2002).

38   The need for a high spatiotemporal DSR has increased noticeably in recent years. For example, high
39   temporal resolution of solar resource data is required by new power system models, such as the Integrated Grid
40   Modeling System (IGMS) (Palmintier et al., 2017). Additionally, information about the short-term fluctuation of
41   DSR is critical for storage analysis of large grid-connected photovoltaic plants through ramp-rate control
42   (Marcos et al., 2014). High spatial resolution DSR data are prerequisites for producing small-scale solar energy,
43   which has received increased attention in recent years (Jain et al., 2017). Hence, the combination of high spatial
44   and temporal DSR estimations is important for the economic and stable operation of the solar grid (Buster et al.,
45   2021). However, because of the comparatively coarse resolution of existing products, the spatial and diurnal
46   variations in DSR at large scales have not been fully studied. Moreover, as the driving parameters of various
47   land models, DSR and PAR data with high spatial and temporal resolutions are essential for estimating many
48   other surface variables at high spatial and temporal scales, such as land surface temperature (Jia et al., 2022a,
49   2022b), ground-level ozone mapping (Wei et al., 2022), and evapotranspiration (Huang et al., 2019).

50   Satellite-based estimation of surface incident shortwave radiation has rapidly developed in recent decades.
51   Polar-orbiting satellite sensors, such as the Moderate Resolution Imaging Spectroradiometer (MODIS), provide

one of the most popular data sources because of their extended global coverage and availability of mature high-level atmospheric and surface products (Liang et al., 2006; Zhang et al., 2014; Zhang et al., 2018). Many existing DSR and PAR products, such as the Breathing Earth System Simulator (BESS) (Ryu et al., 2018), Global Land Surface Satellite Downward Shortwave Radiation (GLASS) (Zhang et al., 2019), and MODIS land surface Downward Shortwave Radiation (MCD18) (Wang et al., 2020) were generated based on MODIS observations. With the future retirement of MODIS, studies have started to focus on estimating DSR from the Visible Infrared Imaging Radiometer Suite as well (Li et al., 2022). An advanced very high-resolution radiometer (AVHRR) is also a valuable data source for DSR estimation owing to its long-term data record (Yang et al., 2018). The Clouds, Albedo, and Radiation Edition 2 (CLARA) data products were based on AVHRR (Karlsson et al., 2017). However, the above-mentioned products usually generate daily DSR by interpolating from instantaneous estimation because of the limited overpass counts of polar-orbiting satellites. Because of their limitation to capture diurnal DSR variation, the root mean square error (RMSE) of these products can hardly reach 25 W/m^2 (Li et al., 2021).

A lot of effort has been made to develop the high temporal resolution DSR estimation. The hourly Earth's Radiant Energy System (CERES) and the International Satellite Cloud Climatology Project HXG product on a three-hour scale (Tang et al., 2019) are generated by incorporating high-level satellite products and other ancillary data set. The unique Lagrange point orbit of Earth Polychromatic Imaging Camera (EPIC) onboard the Deep Space Climate Observatory (DSCOVR) are also utilized to generate hourly DSR and PAR (Hao et al., 2018, 2019). Geostationary sensors provide new opportunities for estimating the DSR and PAR. Previous studies have successfully estimated surface shortwave radiation from geostationary sensors, such as multifunctional transport satellites (Huang et al. 2011; Li et al., 2015) and MSG Spinning Enhanced Visible and InfraRed Imager (Schmetz et al. 2002). With the launch of new-generation geostationary satellites, more studies have shifted to the Advanced Himawari Imager (AHI), Advanced Baseline Imager (ABI), and Advanced Geosynchronous Radiation Imager (AGRI), which provide higher spectral, spatial, and temporal resolutions with geometric and radiometric accuracies comparable to those of their polar-orbiting counterparts. Zhang et al. (2020) estimated the DSR from both AHI and ABI data using an optimization method. Letu et al. (2022) generated a suite of radiation datasets from AHI aerosol and cloud products. However, the RMSE of the hourly DSR estimation based on the above-mentioned methods is generally around 100 W/m^2 and the daily average is still around 25-30 W/m^2. A recent study that employed a machine learning method to estimate half-hourly DSR achieved a validation RMSE of approximately 67 W/m^2, but their validation sites were limited and depended on the training sites (Chen et al., 2021). In addition, although various methods have been developed, no uniform products have been generated based on new-generation geostationary satellites. This is partly due to the differences in the spectral configuration or scan strategy between the carried sensors and the non-transferability of some existing retrieval methods. The requirement of data storage for products with high spatial and temporal resolutions is another reason that impedes the development and generation of such data products.

To address those challenges, we employed the physical-based look-up table (LUT) method, which uses top of atmosphere (TOA) reflectance as the main input and does not rely on high-level atmospheric products, such as aerosol or cloud optical parameters. Hence, it is fast and transferable across different sensors, and eliminate possible data gaps resulted from the unavailability of the high-level atmospheric products. The TOA reflectance data are obtained from the National Aeronautics and Space Administration (NASA) Advanced Supercomputing (NAS) Division GeoNEX platform, which archives a collection of gridded data from multiple geostationary satellites with consistent file formats and map projections (Yip, 2019). The generated GeoNEX DSR/PAR product covers both the AHI and ABI areas in the same format at 1 km and hourly resolution. Compared with existing products, the GeoNEX DSR/PAR product presents the highest accuracy at both hourly and daily scales. This study also took advantage of the high spatial and temporal information provided by the new product and investigated the spatiotemporal variability of DSR. The data product was archived in the NASA GeoNEX data portal. The remainder of this paper is organized as follows: Section 2 introduces the data and methods used to develop the GeoNEX DSR/PAR products; Section 3 presents validation and comparison results for the new data product; Section 4 uses two examples to demonstrate the application of the high spatiotemporal resolution product in investigating DSR variability; Section 5 describes the data products and access information. Finally, Section 6 concludes the study with a summary.

2. Data and method

2.1 Method

This study employs the LUT approach initially developed by Liang et al. (2006). The method was further refined by extending the LUTs, considering the impacts of water vapor and surface elevation, and applied to produce the NASA MODIS DSR/PAR product (MCD18) (Wang et al., 2020). To estimate surface fluxes, two parameterization schemes model the radiative transfer process and simplify the interactions of radiation between

109   the atmosphere and the surface.

110   The first parametrization scheme (Eq. 1) builds the relationship between the TOA spectral reflectance R,
111   surface spectral reflectance r, and three parameters related to atmospheric conditions from the clearest condition
112   to the cloudiest conditions at a given viewing geometry: path reflectance $R_0(\lambda)$, atmospheric spherical albedo
113   $\rho(\lambda)$, and transmittance $\gamma(\lambda)$ for the spectral band. They are functions of the viewing geometry (i.e., solar zenith
114   angle (SZA θ_s), view zenith angle (VZA), and relative azimuth angle (RAA)), water vapor, and elevation. The
115   values of the three parameters were stored in the first LUT.

116   $$R(\lambda) = R_0(\lambda) + \frac{r(\lambda)}{1-r(\lambda)\rho(\lambda)} cos(\theta_s)\gamma(\lambda)/\pi \quad (1)$$

117   The second parameterization scheme (Eq. 2) estimates the surface broadband radiation F from surface
118   reflectance r and three atmospheric parameters: path irradiance F_0, atmospheric spherical albedo ρ, and
119   atmospheric transmittance γ at given θ_s. E_0 is the extra-terrestrial solar broadband irradiance, which is adjusted
120   by the distance to the sun. The second LUT was built to retrieve three atmospheric parameters with known SZA:
121   water vapor, elevation, and visibility index retrieved from the first LUT.

122   $$F = F_0 + \frac{r\rho}{1-r\rho} E_0 cos(\theta_s)\gamma \quad (2)$$

123   To generate hourly DSR and PAR, we first calculated the instantaneous visibility index at 10- or 15-
124   minutes (the refreshing frequency of a satellite sensor) by comparing the actual TOA radiance from the sensor
125   with the series of simulated radiances stored in the first LUT (Eq.1). The visibility indexes were then averaged
126   to the hourly interval. Hourly DSR and PAR were estimated by searching for the second LUT using the hourly
127   averaged visibility index.

128   **2.2 Data**

129   **2.2.1 Input data**

130   The input variables and corresponding data sources are listed in Table 1. The gridded TOA reflectance of
131   the ABI and AHI and the corresponding viewing geometry data were archived through the NASA GeoNEX data
132   portal (Wang et al., 2020). The ABI onboard the GOES-16 geostationary meteorological satellites is equipped
133   with 16 spectral bands. It produces full disk scanning every 10 or 15 min covering the area from 60°N, 138°W,
134   to 60°S, 18°W. The AHI onboard Himawari-8 has 16 spectral bands. It produces full disk scanning every 10
135   min, covering regions from 60°N, 78°E to 60°S, 198°E. The blue band with a central wavelength of 0.47 um
136   and 1 km spatial resolution for both ABI and AHI was used in this study to infer the atmospheric visibility
137   index. The MCD43 and surface reflectance climatology products provided surface albedo information. The
138   surface reflectance was obtained from the MODIS product (Schaaf & Wang, 2015). Climatological surface
139   reflectance data were used when no valid MODIS observation was available (Jia et al., 2022). The total column
140   water vapor data were retrieved from MERRA2 (Global Modeling and Assimilation Office, 2015), and the
141   surface elevation data were obtained from the Global 30 Arc-Second Elevation (GTOPO30) (EROS, 2017).

142   Table 1. The summary of input data

Name	Variable	Spatial Resolution	Temporal Resolution
AHI/ABI TOA reflectance	TOA reflectance	1km	15min or 10min
View geometry	Solar zenith angle, sensor zenith angle, relative azimuth angle	1km	15min or 10 min
MCD43C3	Surface albedo	0.05 degree	Daily
MERRA2	Total column water vapor	0.5 x 0.625 degree	Hourly
GTOPO30	Surface elevation	30 arc seconds	Static
Surface reflectance climatology	Surface reflectance	0.05 degree	Static/daily

143

144   **2.2.2 Validation data**

145   Measurements from 63 stations in the ABI or AHI spatial domain were collected to validate GeoNEX
146   DSR/PAR products. Among these, 34 sites were located in the ABI coverage domain and 29 sites in the AHI
147   coverage area (Fig. 1). The stations belong to four networks, with 25 sites from AMERIFLUX, 11 sites from the
148   Baseline Surface Radiation Network (BSRN), 20 sites from FLUXNET, and 7 sites from the Surface Radiation

149 Network (SURFRAD). All 63 sites had DSR data. The processes of ground measurement data quality checks
150 including daily and monthly aggregation follow Li et al. (2021). Only 27 sites recorded PAR measurements.
151 Seven sites from SURFRAD measure the PAR flux directly while the rest sites from AMERIFLUX record PAR
152 data in quantum units (photosynthetic photon flux density, $\mu mol\ m^{-2}s^{-1}$). The conversion between the
153 quantum units to the energy units follows Dye (2004).

154
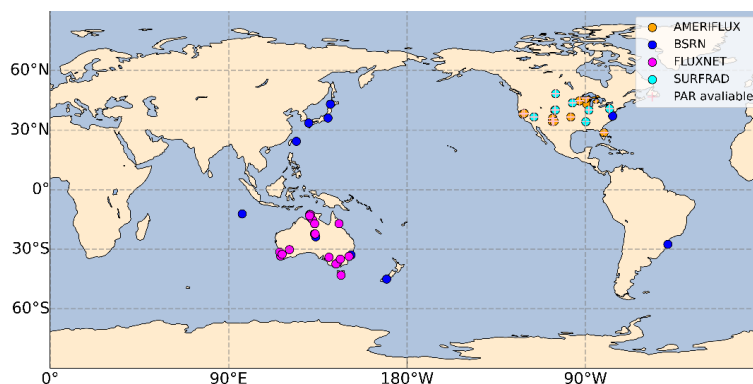
155
156 Figure 1. The map of ground stations used for validating the GeoNEX DSR/PAR product.
157

158 **2.2.3 Other products**

159 Existing DSR products were used in this study for comparison with the new GeoNEX product. The
160 EPIC/DSCOVER generates DSR and PAR globally at 0.1° spatial resolution and 1-2h temporal resolution. A
161 random forest approach was applied to the data obtained by the EPIC sensor onboard the DSCOVER (Hao et al.,
162 2018, 2019). The CERES SYN1deg product provides hourly, 3hourly, daily, and monthly radiation data at the
163 surface, TOA, and various atmospheric layers with a 1° spatial resolution. The data on surface shortwave fluxes
164 were calculated with Langley Fu-Liou radiative transfer code from polar-orbit and geostationary satellite data, as
165 well as other ancillary information (Rutan et al., 2015). CERES-SYN data has been extensively validated in
166 previous studies, showed the highest accuracy compared with the most existing products; hence, it has been widely
167 used as a baseline product (Riihelä et al., 2017; Sun et al., 2018; Li et al., 2021). The National Oceanic and
168 Atmospheric Administration (NOAA) GOES-R series Level 2 product (ABI-L2-DSR) was also evaluated in this
169 study. The full disk data were produced on a global latitude/longitude grid at 0.5° resolution, employing two
170 retrieval path methods to estimate DSR (GOES-R Algorithm Working Group and GOES-R Program Office,
171 2017). A new version of MCD18A1 has also been included in the comparison (Wang et al., 2020). It applied a
172 similar LUT method over MODIS TOA reflectance and estimated DSR at a global scale at 1 km spatial resolution
173 with 3hourly and daily interpolated temporal resolutions.

174 In addition, this study employed NOAA GOES-R Series Level 2 clear sky mask data to investigate the
175 performance of various DSR/PAR products under different cloud conditions. The product contains images in the
176 form of binary cloud masks. To match it with hourly DSR products, the 15 min full disk data were aggregated.
177 The sample was classified as under cloudy conditions if all four observations in an hour were cloudy and as clear
178 if all four observations within an hour were clear. The rest were classified as partial cloudy conditions.

179 **3. Quality assessment**

180 **3.1.1 Overall validation**

181 Both hourly and daily GeoNEX DSR were validated with ground measurements, as shown in the scatter
182 plots of the ABI and AHI domains (Fig. 2). The R^2 values for the hourly validations of ABI and AHI were
183 0.929 and 0.950, respectively. RMSE were 78.2 and 69.4 W/m^2 and relative RMSE (rRMSE) were 19.7% and
184 16.2%. After aggregating to the daily values, the uncertainties in estimating DSR were further reduced, while
185 the R^2 increased to 0.968 and 0.972 for ABI and AHI, respectively. The RMSE (rRMSE) achieved 18.4 (9.6%)
186 and 17.2 (8.3%) W/m^2. To the best of our knowledge, it is the first satellite product of DSR with the rRMSE
187 lower than 10% (Li et al., 2021). The validation accuracies over ABI and AHI coverage are similar, with
188 slightly better accuracy over AHI. This is partly due to the more homogeneous and constant atmospheric
189 conditions in the AHI domain. After aggregating into daily intervals, the differences between the two sensors
190 decreased. The accuracy of the DSR estimation varies with cloud conditions. As shown in Fig. 3, the rRMSE

191   over cloudy sky (30.6%) is triple that over clear sky (10.9%), and the rRMSE of partial cloud samples (18.3%)
192   fell in the middle of accuracies under clear and cloudy skies. The elevated errors for cloudy-sky cases partly
193   originate from the assumption of homogenous and plane-parallel clouds in the radiative transfer code (Chen et
194   al., 2019; Van Laake & Sanchez-Azofeifa, 2004). The linear interpolation processes in searching through the
195   two LUTs may also lead to uncertainties in the results.

196   Figure 4 presents the validation results of the GeoNEX PAR estimation. The R^2 for hourly PAR estimation
197   was 0.927, and the RMSE (rRMSE) was 34.7 (19.7%) W/m^2. The R^2 for daily estimation was 0.956, and the
198   RMSE (rRMSE) was 9.5 (10.8%) W/m^2. Since the PAR values of some sites are converted from the
199   photosynthetic photon flux density which has systematic uncertainties (Dye, 2004), we also include the
200   validation results only over SURFRAD sites where PAR flux is provided directly. The accuracies of both hourly
201   and daily PAR estimations were higher than those of the existing products and experimental studies (Li et al.,
202   2015; Hao et al., 2018).
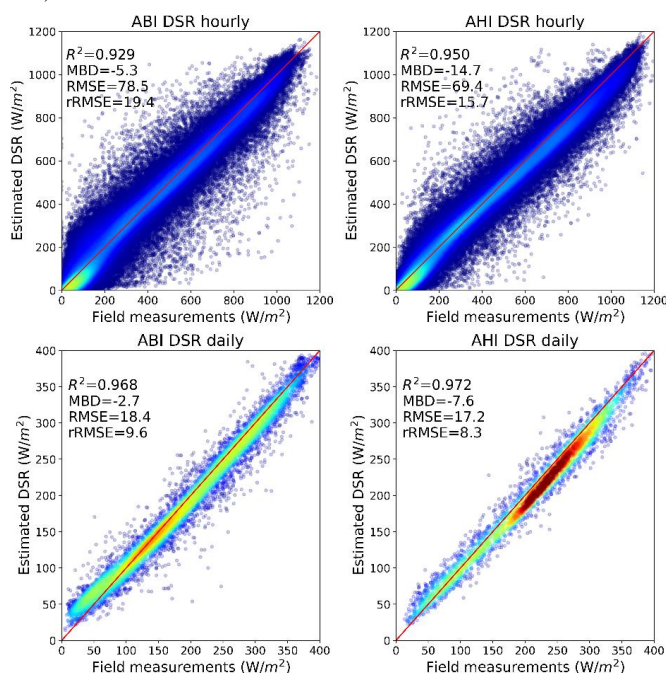
203
204   Figure 2. Scatter plots of the estimated and observed daily and hourly DSR values for ABI and AHI data.
205
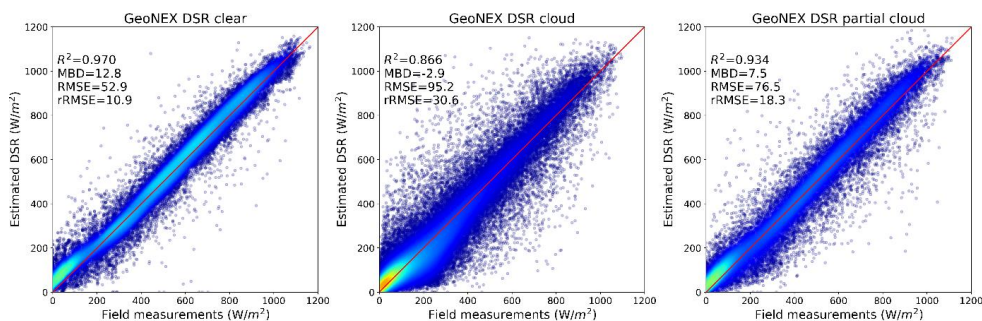
206
207   Figure 3. Scatter plots of the estimated and observed hourly DSR values for ABI coverage under different cloud
208   conditions
209
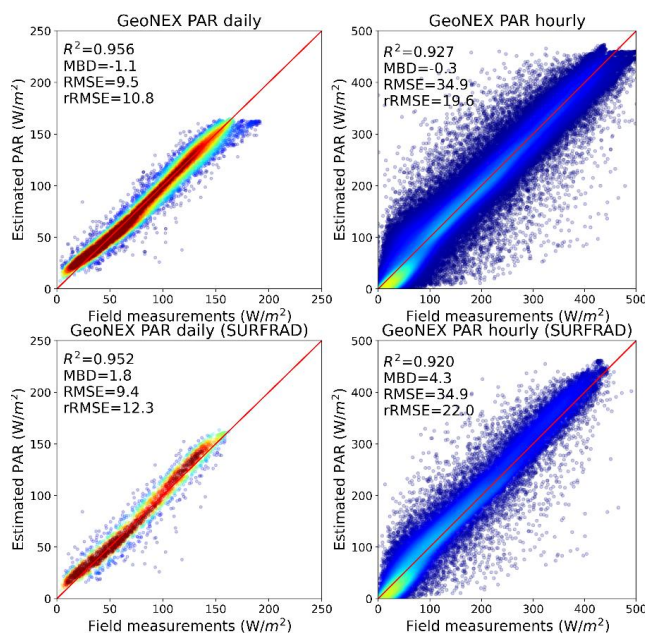
210
211   Figure 4. Scatter plots of the estimated and observed daily and hourly PAR values for ABI coverage

212   **3.1.2   Comparison with existing products**

213   We also compared the new GeoNEX DSR product with four existing DSR products at hourly and daily
214   scales over identical samples. The statistics are summarized in Table 2. The correlation between the CERES
215   hourly DSR product and the ground measurements had an R^2 value of 0.904 and RMSE of 91.6 W/m^2,
216   followed by EPIC/DSCOVER with $R^2 = 0.798$ and RMSE = 130.8 W/m^2. ABI-L2-DSR had an R^2 value of
217   0.748 and RMSE of 148.8 W/m^2. The proposed GeoNEX DSR outperformed all existing products (Letu et al.,
218   2022; Zhang et al., 2021; Hao et al., 2019) with R^2 of 0.928 and RMSE of 78.3 W/m^2. The relatively lower
219   performance of the ABI-L2-DSR data may be partly because the ABI-L2-DSR is an instantaneous estimation
220   and has a coarse spatial resolution of 0.5 °. Table 3 presents a comparison of hourly products under different
221   cloud conditions. CERES and GeoNEX achieved comparable accuracy under clear-sky conditions. Over cloudy
222   skies, the GeoNEX product exhibits superior accuracy with an RMSE of 95.2 W/m^2. The RMSE of CERES
223   and EPIC were as high as 112.8 and 159.0 W/m^2, respectively.

224   For daily estimation, MCD18, which retrieves DSR from the polar orbiting sensor at the highest spatial
225   resolution of 1 km, was also included in comparison with CERES and EPIC. Other mature daily DSR products,
226   such as GLASS, CLARA, and BESS, were not included in this study because they have shown comparable or
227   inferior performance to CERES (Li et al., 2021). Similar to the hourly results, GeoNEX DSR outperformed all
228   existing datasets with R^2 of 0.965 and RMSE of 18.9 W/m^2.

229   We emphasize that the GeoNEX DSR/PAR algorithm was not trained or tuned with the field
230   measurements used for comparison. The validation and comparison results show that this new GeoNEX
231   shortwave radiation product provides a highly accurate DSR estimation from satellites, with hourly RMSE
232   lower than 80 W/m^2 and daily RMSE lower than 20 W/m^2.

233   Table 2. Summary of the comparison results between the GeoNEX DSR product and other DSR products

Product	R^2	BIAS (W/m^2)	RMSE (W/m^2)
		Instantaneously	
ABI-L2-DSR	0.75	-13.9	148.8
		Hourly	
CERES	0.90	2.7	91.6
EPIC	0.80	2.8	130.8

GeoNEX	0.93	-3.4	78.3
	Daily		
CERES	0.94	3	24.5
MCD18	0.91	-5.2	32.6
ABI-L2-DSR	0.77	-7.4	48.1
EPIC	0.83	5.9	41.5
GeoNEX	0.97	-2.4	18.9

234

235 Table 3. Comparison of the GeoNEX DSR product with other DSR products under different cloud conditions.

Product	R^2	BIAS (W/m^2)	RMSE (W/m^2)	R^2	BIAS (W/m^2)	RMSE (W/m^2)	R^2	BIAS (W/m^2)	RMSE (W/m^2)
	clear			cloud			partial cloud		
CERES	0.97	-11.1	52.4	0.82	19.0	112.8	0.91	-10.1	91.8
EPIC	0.94	-45.8	86.2	0.69	50.7	159.0	0.85	-15.6	115.9
GeoNEX	0.97	-12.8	52.9	0.87	2.9	95.2	0.93	-7.5	76.5

236

237 To evaluate their capability to monitor the temporal variability of DSR, the diurnal cycles of GeoNEX,
238 EPIC, and CERES DSR estimations were plotted together with in-situ measurements at seven SURFRAD sites
239 in June 2018 (Fig. 5). Although all three products could depict the diurnal trends of DSR, their performances
240 diverged substantially over the days with high DSR variability (i.e., days of year (DOY) 174 and 175) and
241 mountainous areas (i.e., TBL). EPIC was prone to overestimation when potential clouds existed. CERES agreed
242 well with the in-situ measurements, but could not capture the sharp changes in DSR as accurately as GeoNEX
243 due to coarse spatial resolution of CERES data.

244
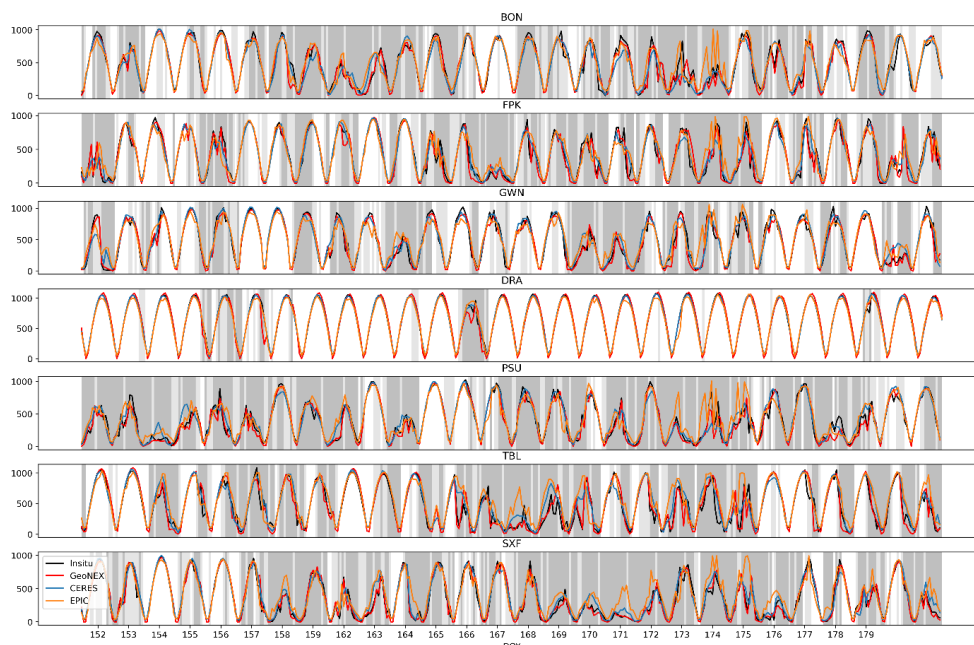
245
246 Figure 5. The diurnal cycles of GeoNEX, EPIC, and CERES estimations compared with in-situ measurements at
247 seven SURFRAD sites in June 2018. Cloudy conditions are marked in dark grey and partially cloudy conditions
248 are light grey.

249 **3.1.3   Impact of viewing geometry on estimation errors**

250 The diurnal variation of the GeoNEX DSR estimation was examined and is presented in Fig. 6. The hourly

Earth System
Science
Data

251 averaged DSR matched well with the in-situ measurements for both ABI and AHI. No noticeable changes in the
252 RMSE and BIAS were observed throughout the day. However, owing to the small average DSR values at the
253 start and end of a day, the rRMSE increases dramatically. This phenomenon occurs in most DSR products,
254 partly due to the Lambertian assumption adopted in the radiative transfer model.

255
256
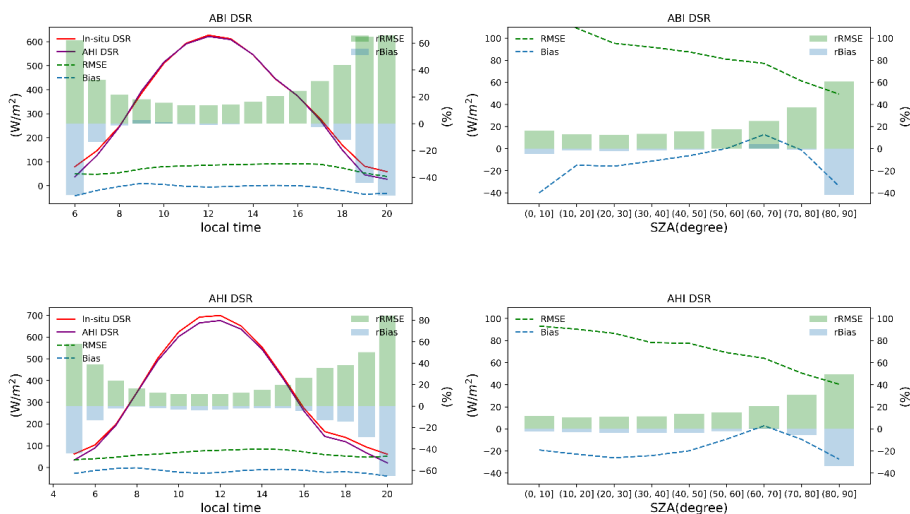
257
258 Figure 6. The diurnal variation and the impact of SZA on AHI and ABI DSR estimation

259 Geostationary satellites maintain a static position relative to the Earth, and thus each pixel in the image has
260 a fixed value of VZA. Figure 7 presents the rRMSE and rBias of each site located under AHI and ABI coverage.
261 The pink stars represent the positions of the AHI and ABI sensors. For the rRMSE, a radial distribution is
262 presented. A large rRMSE existed at sites far from the sensors. The same result was obtained for the rBias
263 distribution. Underestimation was observed over the sites near the sensor, whereas overestimation was observed
264 for sites far from the sensor. Overall, more uncertainties may exist at higher latitudes, as the geostationary
265 sensors are located at the equator. To quantitatively analyze the influence of VZA, regression lines between
266 VZA and rRMSE/rBias are plotted in Fig. 8. Positive slopes exist for both rRMSE and rBias. The p-values for
267 both the rRMSE and rBias are less than 5%, which demonstrates that these positive correlations are significant.
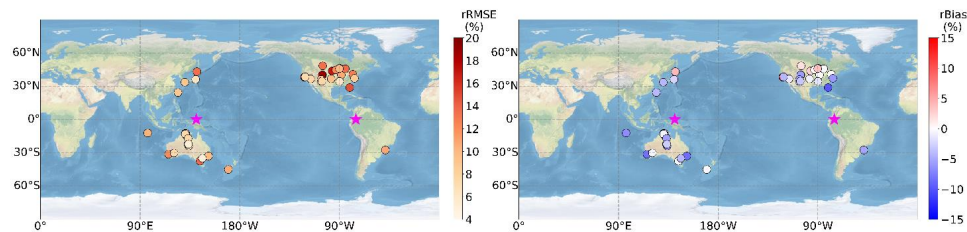
268
269 Figure 7. The spatial distribution of rRMSE and rBIAS of DSR estimation. The pink stars represent the position
270 of the AHI and ABI sensors.

271
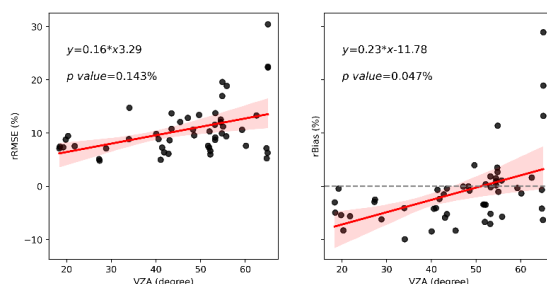
272
273 Figure 8. The impact of VZA on DSR estimation. The regression equation and p-value are shown.
274

3.1.4 Impact of spatial and temporal resolutions on estimation errors

276   Previous studies have suggested that the accuracy of DSR estimation is influenced by the spatial and
277 temporal aggregation scales (Li et al., 2021; Zhang et al., 2021). For instantaneous PAR and DSR estimation,
278 the optimal scale for applying 1-D transfer models is approximately 20 km (Chen et al., 2019; Zhang et al.,
279 2021). For daily estimation, Li et al. (2021) demonstrated that generally lower spatial resolution can result in
280 higher accuracy for most existing products, but it is noticeable that the products validated in previous studies are
281 usually interpolated from instantaneous estimation. To further examine the influence of spatial and temporal
282 resolution on surface shortwave radiation estimation, this study compared the accuracy of DSR estimation at
283 different scales (Fig. 9 and Table 4). This agrees well with previous findings that temporal aggregation exerts a
284 greater impact on accuracy than spatial aggregation (Zhang et al., 2021). The hourly rRMSE was approximately
285 18%, while the monthly are approximately 6%. The higher the temporal resolution, the greater the influence of
286 the spatial resolution on the estimation accuracy. As shown in Fig. 9, the differences in RMSE among different
287 spatial resolutions decreased as the temporal resolution decreased. At the hourly scale, the highest rRMSE
288 reached 19.8% at 100 km and the lowest was 17.1% at 10 km, whereas at the monthly scale, the DSR estimation
289 was nearly independent of the spatial scale. Moreover, compared with previous analysis of instantaneous
290 interpolated daily DSR estimation (Li et al., 2021), our results at a daily scale are less variable among different
291 spatial scales, suggesting that the aggregation of hourly DSR is a possible solution to mitigate the impact of
292 spatial resolution on daily DSR estimation and enables daily DSR estimation at spatial resolutions as high as 1
293 km.
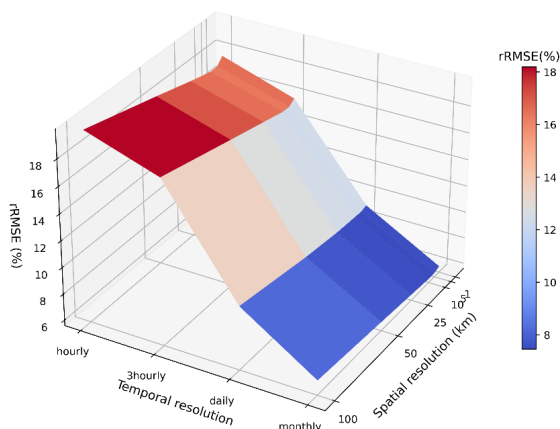
294
295 Figure 9. Influence of spatial and temporal resolution on DSR estimation
296
297 Table 4. Summary of spatial and temporal influence on hourly and daily DSR estimation.
298

Resolution	R^2	BIAS (W/m^2)	RMSE (W/m^2)	R^2	BIAS (W/m^2)	RMSE (W/m^2)
		Hourly			Daily	

1km	0.94	-9.4	74.3	0.97	-4.3	18.0
5km	0.94	-9.8	72.2	0.97	-4.4	17.7
10km	0.94	-9.3	72.0	0.97	-4.4	17.8
25km	0.94	-8.8	73.9	0.97	-4.1	18.0
50km	0.93	-8.7	77.2	0.97	-4.1	18.6
100km	0.92	-8.4	83.8	0.96	-4.0	20.4

299

4. Application demonstrations

301 The importance of spatial and temporal heterogeneity of the DSR has been demonstrated in many studies
302 (Gueymard et al., 2011; Yan et al., 2018; Sweerts et al., 2019). However, such issues have not been fully
303 investigated owing to the limited spatial and temporal resolutions as well as relatively low accuracy of the
304 existing products. The new GeoNEX DSR/PAR product, with their unique characteristics, provide a valuable
305 opportunity to re-examine these issues. Here, two examples are used to demonstrate the applications of the high
306 spatial-temporal resolution DSR product. In Section 4.1, we investigated how the overpass time and counts of
307 polar-orbiting satellites affect the accuracy of estimating the daily DSR values. In Section 4.2 we studied the
308 spatial heterogeneity of DSR at various temporal scales.

4.1 Effects of overpass time on estimating daily DSR

310 The quality of existing DSR products derived from polar-orbiting satellite data relies heavily on temporal
311 upscaling schemes to calculate the daily DSR from instantaneous observations (Wang et al., 2010). We took
312 advantage of the high frequency of the GeoNEX DSR product to simulate how the estimates of daily DSR
313 change with overpass time and counts.

314 The modislike11 and modislike13 data are generated using visibility indexes at local times 11:00 and
315 13:00, corresponding to the Terra and Aqua passing time, as the constant atmospheric condition of the whole
316 day. The Modislike2p data were generated to emulate the cases where observations from both Terra and Aqua
317 are available. It uses the visibility index at 11:00 to represent the atmospheric condition before 11:00 and the
318 visibility index at 13:00 to represent that after 13:00. Between 11:00 and 13:00, The visibility index was linearly
319 interpolated (Wang et al., 2010). A similar interpolation method was used to generate the MCD18 products
320 (Wang et al., 2020). The mechanism is shown in Fig. 10, where different data were compared over the seven
321 SURFRAD stations on June 19th. The results show that all methods work well under no-cloud conditions, such
322 as at the DRA site, where the visibility index at 13:00 and 11:00 can represent the entire day's atmospheric
323 condition. However, large uncertainties arise when atmospheric conditions vary substantially during the day.
324 Such uncertainties may be reduced with additional observations in the modislike2p scenario, as in the case of
325 the PSU. Nevertheless, the limited number of observations is one of the major error sources for estimating the
326 daily DSR from polar-orbiting satellite data.
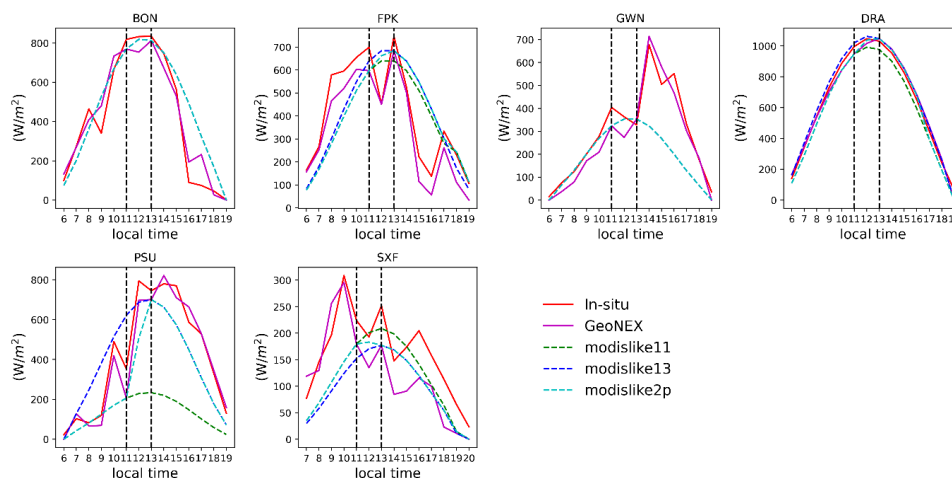
327
328 Figure 10. Comparison between modislike hourly DSR and GeoNEX DSR over seven SURFRAD stations on
329 June 19th.

330   The relative bias (rBias) and RMSE (rRMSE) of the daily averaged DSR between modislike interpolated
331   data and ABI data throughout the year were calculated (Fig. 11). The rBias maps showed that the
332   representativeness of the visibility index at 11:00 varied spatially. More overestimations were observed over
333   high-elevation areas, and underestimations were observed at the edge of these areas, which may be because the
334   morning clouds have not been formed or could not reach certain heights. Moreover, the visibility index at 13:00
335   h was not sufficiently representative. The rBias map shows that interpolation from the visibility index at 13:00
336   will lead to underestimation over all study areas, which is attributed to more cloud formation in the afternoon.
337   The rRMSE maps demonstrate the efficiencies of incorporating two passes when interpolating daily DSR from
338   polar-orbiting sensors, as the modislike2p generates less variability compared with ABI-based daily DSR;
339   however, the average rRMSE reaches 10%. For both modislike10 and modislike 13, the high rRMSE is around
340   the mountainous areas, the maximum rRMSE is approximately 70%, and the average rRMSE is approximately
341   18%.

342
343
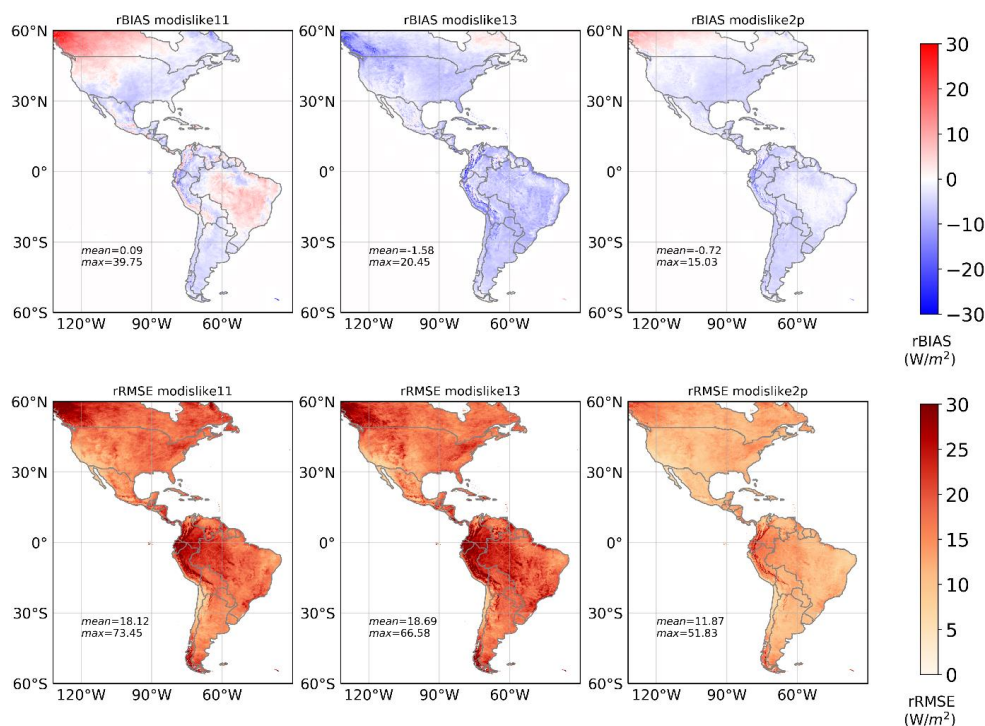
344
345   Figure 11. The temporal representation maps are generated by calculating rBias and the rRMSE between
346   modislike10, modislike13, and modislike2p daily interpolated data and ABI data.

347

348   **4.2   Spatial heterogeneity of DSR**

349   Existing global or regional shortwave radiation products mostly have a spatial resolution coarser than 5
350   km, which meets the requirements of some terrestrial models. However, other studies may require data with a
351   much higher spatial resolution. For instance, whether the character of a solar resource at one location can be
352   representative of nearby locations is a critical question for solar grid design and deployment. Attempts have
353   been made to analyze the spatial heterogeneity of DSR, but most have focused on regional scales or used coarse
354   resolution data as inputs (Kariuki & Sato, 2018; Sarr et al., 2021; Tapia et al., 2022). With the help of the high
355   spatiotemporal resolution GeoNEX DSR data, we were able to quantify the spatial heterogeneity of DSR at a
356   large spatial scale over different temporal scales.

357   We employed the metric used in the previous studies (Gueymard et al., 2011; Yan et al., 2018) to calculate
358   the coefficient of variance (COV) to represent spatial heterogeneity of DSR. COV is defined as:

359
$$COV = \frac{\sigma_n}{E_n} * 100$$

360 where n denotes the number of pixels surrounding the central pixel. N was set as 10×10 and 100×100 km,
361 respectively, to examine spatial heterogeneity at different scales. σ_n and E_n are the standard deviation and mean
362 of these n pixels, respectively.

363   Annual and seasonal spatial representation maps were generated at 10×10 and 100×100 km, which
364 highlight areas susceptible to high heterogeneity in the DSR (Fig. 12). A high COV usually corresponds to
365 mountainous and high elevation areas. For the annual COV in the 10×10 matrix over CONUS, the lowest COV
366 occurs in central Missouri and increases towards the east and west coasts. Some regions at the edge of the
367 American Cordillera, such as Denver, have a high COV. A high COV extends from northern Rocky in Canada
368 along the American Cordillera to Mexico and further reaches the entire Andes Mountains in South America.
369 Over Asia and Oceania under the AHI coverage (Fig. 12), a high COV is present at the edge of the Tibetan
370 Plateau, especially along the Himalayan Mountains and extends to the Annamite range. It also occurs in
371 mountainous regions of island countries such as Indonesia, Japan, and New Zealand. The patterns between
372 10×10 km and 100×100 km were similar, with greater variability and extent in the latter representation maps.
373 Larger COV pixels appear along the Appalachian Mountains in the US, eastern mountainous areas in Brazil, the
374 northern part of the Tibetan Plateau in China, and southeast Australia. The analysis here suggests the need for
375 high-spatial-resolution DSR data for these regions. Some seasonal changes in the COV values were also
376 observed. We plotted aggregated June, July, and August (JJA) as well as December, January, and February
377 (DJF) aggregated variation maps, as shown in Fig. 12. In general, a higher variance was observed in the
378 Northern Hemisphere during DJF and in the Southern Hemisphere during JJA. It impacts high latitude most. It
379 is also noticeable that a horizontal line appears at approximately 55°N in both AHI and ABI 100×100km maps
380 during DJF. This might correspond to the polar front where a sharp gradient in temperature occurs and suggests
381 that these two air masses with different temperatures leads to significant DSR variation at the surface at a 100
382 km scale.
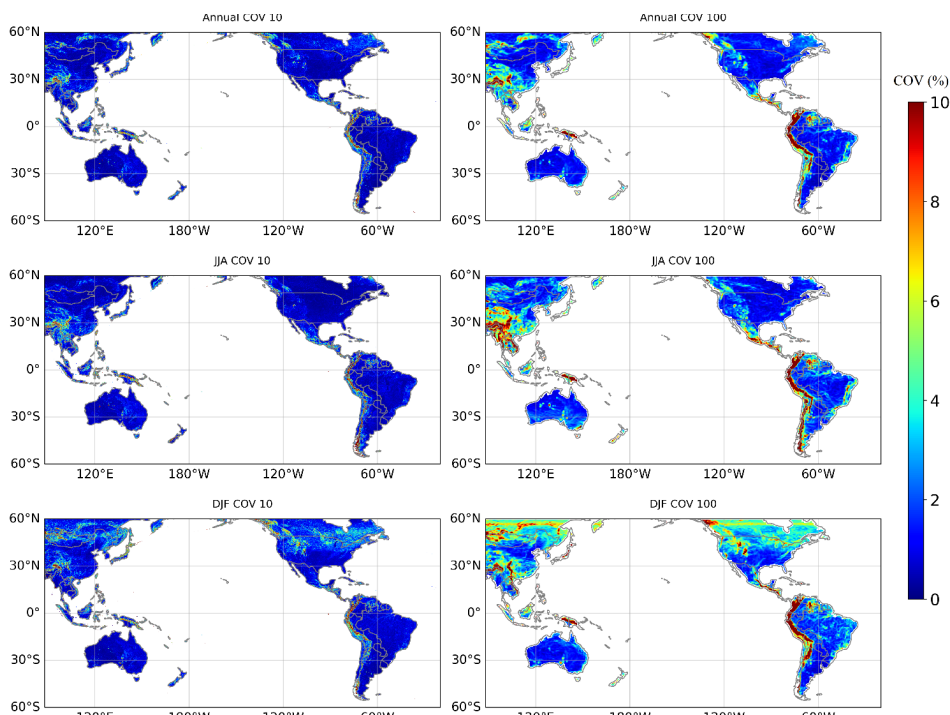
383
384 Figure 12. Spatial representation maps at 10km and 100km scales during June, July, August (JJA) and
385 December, January, and February (DJF)

386   Figure 13 shows the distribution of daily and hourly COV frequencies at 10 and 100 km in all study areas.
387 For the daily COV at 100 km, 86% of the areas were within the range of 3%-10%. For daily COV at 10 km,

388   85% of areas showed a COV lower than 3%, and most areas had a COV distributed within the range of 2%-3%.
389   For the hourly COV at 100 km, 73% of the areas had a COV higher than 5%, and most areas were distributed
390   within 20%-30%. For the hourly COV at 10 km, 64% of the areas had a COV within the range of 3%-10%. The
391   values between 5%-10% were dominant for COV. The results demonstrate that the higher the temporal
392   resolution, the more severe the spatial heterogeneity issues. DSR products with spatial resolutions of
393   approximately 100 km are not sufficient for analysis at temporal scales higher than daily for most areas. The 10
394   km DSR products may be sufficient for analysis using daily DSR data, but for those with hourly data,
395   uncertainties in COV of 5%-10% existed for most areas. The results further demonstrate the importance of high-
396   spatial-resolution products, particularly at high temporal resolution.

397

398
399
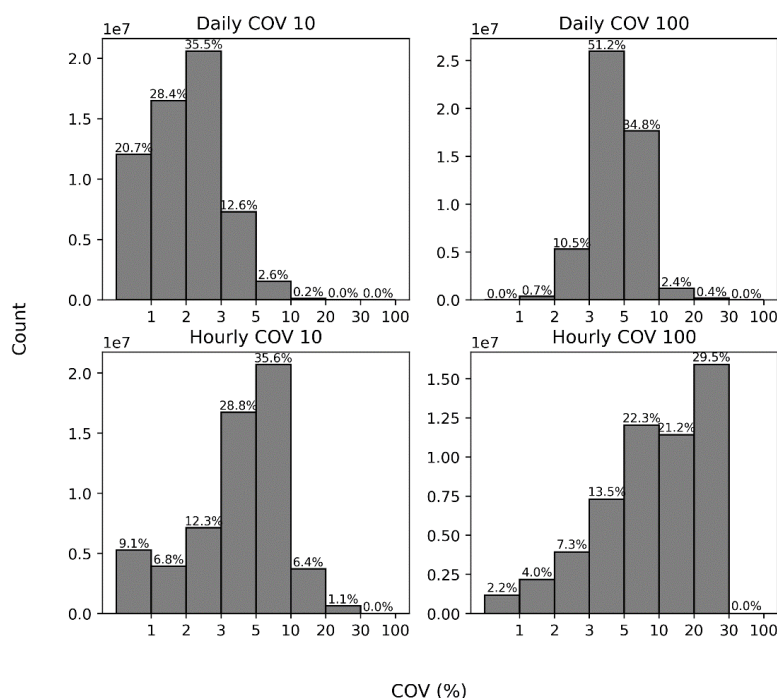
400
401   Figure 13. Histogram of daily and hourly COV at 10km and 100km. The number above the bar indicates the
402   relative frequency.

403   **5.   Data availability**

404   The GeoNEX DSR/PAR data product can be downloaded from
405   https://data.nas.nasa.gov/geonex/geonexdata/GOES16/GEONEX-L2/DSR-PAR/ and
406   https://data.nas.nasa.gov/geonex/geonexdata/HIMAWARI8/GEONEX-L2/DSR-PAR/
407   (https://doi.org/10.5281/zenodo.7023863, Wang & Li, 2022). It is a gridded product organized in a tile system
408   that follows the convention of standard GeoNEX data sets. Each tile contains 600x600 pixels, representing a
409   region of 6° by 6°. Detailed information regarding the gridding system can be found at
410   https://www.nasa.gov/geonex/dataproducts. Each file contains three scientific datasets: the DSR hourly array,
411   PAR hourly array, and quality control (QC) array. Users should use the filling value of -9999 to check whether
412   DSR/PAR is successfully retrieved. The DSR or PAR values should be multiplied by a scale factor (0.1) before
413   use. The QC was used to indicate the input source of the surface reflectance data (0 labeled data from the
414   MODIS product and 1 from climatology data).

415   **6.   Conclusions**

416   A gridded high spatiotemporal resolution product of DSR and PAR was produced from new-generation
417   geostationary ABI and AHI data archived through the NASA GeoNEX platform using a physical-based LUT

approach. Hourly DSR and PAR were estimated at 1km resolution over the ABI and AHI coverage domains (60°N to 60°S, 78°E to 18°W). Validation demonstrated that the new GeoNEX DSR and PAR products were highly reliable. The RMSE of hourly DSR estimation is 74.3 W/m^2 (18.0%) and that of daily DSR estimation is 18.0 W/m^2 (9.2%) when evaluated against 63 sites from four different networks. The hourly PAR achieves 34.9 W/m^2 (19.6%) and daily PAR achieves 9.5 W/m^2 (10.5%) validated over 27 sites. It should be noted that the GeoNEX DSR and PAR data were retrieved using a physical LUT approach and did not require any training or tuning based on any of the validation sites. The independent validation results suggest the superior accuracy of the new data product over other existing products, such as CERES, MCD18, EPIC, and NOAA-L2-DSR.

The high-quality gridded dataset of surface incident shortwave radiation provides new opportunities to study its spatial and temporal variability. We demonstrate the application of this new product using two examples. We first mapped the errors in estimating the daily DSR from the polar-orbit satellite data. It was found that one observation per day led to an average relative RMSE of 18 %, and an increase in the daily observation number to two reduced the relative RMSE to 10%. In addition, we characterized the spatial heterogeneity of the DSR based on the new GeoNEX DSR product. It was shown that mountainous and high-latitude areas are more susceptible to high spatial-temporal variation. DSR products with a resolution of approximately 100 km are insufficient for daily and monthly analyses. Analysis at an hourly temporal scale requires DSR data with spatial resolutions finer than 10 km.

Author Contribution

RL: Data curation, Formal analysis, Investigation, Methodology, Writing - original draft, Writing - review & editing. DW: Conceptualization, Funding acquisition, Supervision, Data curation, Formal analysis, Methodology, Writing - review & editing. WW and RW: Funding acquisition, Resources, Writing - review & editing.

Competing interests

The contact author has declared that neither they nor their co-authors have any competing interests.

Acknowledgements

We would like to thank the AMERIFLUX, Baseline Surface Radiation Network (BSRN), Surface Radiation Network (SURFRAD), and FLUXNET for maintaining and providing their measurement data. We would also like to acknowledge the NASA GeoNEX Earth Exchange data portal for providing the gridded AHI and ABI TOA reflectance data, NASA MODIS Land Science Team for providing MCD43 data, NASA Goddard Earth Sciences Data and Information Services Center for providing MERRA-2 data, and Earth Resources Observation And Science Center for providing the GTOPO30 data. The surface albedo climatology data are downloaded from http://glass.umd.edu/albedo_clim/albedo_climatology_0.05CMG/.

References

Buster, G., Rossol, M., Maclaurin, G., Xie, Y., and Sengupta, M.: A physical downscaling algorithm for the generation of high-resolution spatiotemporal solar irradiance data, Solar En(Earth Resources Observation and Science (EROS) Center 2017) ergy, 216, 508-517, https://doi.org/10.1016/j.solener.2021.01.036, 2021.

Chen, L., Yan, G., Wang, T., Ren, H., Hu, R., Chen, S., and Zhou, H.: Spatial scale consideration for estimating all-sky surface shortwave radiation with a modified 1-D radiative transfer model. IEEE Journal of Selected Topics in Applied Earth Observations and Remote Sensing, 12, 821-835, https://doi.org/10.1109/JSTARS.2019.2896644, 2019.

Dye, D.: Spectral composition and quanta-to-energy ratio of diffuse photosynthetically active radiation under diverse cloud conditions, J. Geophys. Res., 109, D10203, https://doi.org/10.1029/2003JD004251, 2004.

Earth Resources Observation And Science (EROS) Center: Global 30 Arc-Second Elevation (GTOPO30), U.S. Geological Survey [Data set], https://doi.org/10.5066/F7DF6PQS, 2017.

Global Modeling And Assimilation Office, and Pawson, S.; MERRA-2 tavg1_2d_slv_Nx: 2d,1-Hourly, Time-Averaged, Single-Level, Assimilation, Single-Level Diagnostics V5.12.4 [Data set]. NASA Goddard Earth Sciences Data and Information Services Center. https://doi.org/10.5067/VJAFPLI1CSIV, 2015.

GOES-R Algorithm Working Group and GOES-R Program Office: NOAA GOES-R Series Advanced Baseline

Imager (ABI) Level 2 Downward Shortwave Radiation: Surface. NOAA National Centers for Environmental Information, 2017.

Gueymard, C. A. and Wilcox, S. M.: Assessment of spatial and temporal variability in the US solar resource from radiometric measurements and predictions from models using ground-based or satellite data. Solar Energy, 85(5), 1068-1084, https://doi.org/10.1016/j.solener.2011.02.030, 2011.

Gu, L., Baldocchi, D., Verma, S. B., Black, T. A., Vesala, T., Falge, E. M., and Dowty, P. R.: Advantages of diffuse radiation for terrestrial ecosystem productivity. Journal of Geophysical Research: Atmospheres, 107(D6), ACL-2, https://doi.org/10.1029/2001JD001242, 2002.

Hao, D., Wen, J., Xiao, Q., Wu, S., Lin, X., You, D., and Tang, Y.: Impacts of DEM geolocation bias on downward surface shortwave radiation estimation over clear-sky rugged terrain: A case study in Dayekou Basin, China. IEEE Geoscience and Remote Sensing Letters, 16(1), 10-14, https://doi.org/10.1109/LGRS.2018.2868563, 2018.

Hao, D., Asrar, G. R., Zeng, Y., Zhu, Q., Wen, J., Xiao, Q., and Chen, M.: Estimating hourly land surface downward shortwave and photosynthetically active radiation from DSCOVR/EPIC observations. Remote Sensing of Environment, 232, 111320, https://doi.org/10.1016/j.rse.2019.111320, 2019.

Hao, D., Asrar, G. R., Zeng, Y., Zhu, Q., Wen, J., Xiao, Q., and Chen, M.: DSCOVR/EPIC-derived global hourly and daily downward shortwave and photosynthetically active radiation data at 0.1° × 0.1° resolution, Earth Syst. Sci. Data, 12(3), 2209–2221, https://doi.org/10.5194/essd-12-2209-2020, 2020.

Huang, G., Ma, M., Liang, S., Liu, S., and Li, X. (2011). A LUT-based approach to estimate surface solar irradiance by combining MODIS and MTSAT data. Journal of Geophysical Research: Atmospheres, 116(D22), https://doi.org/10.1029/2011JD016120, 2011.

Huang, G., Li, Z., Li, X., Liang, S., Yang, K., Wang, D., and Zhang, Y.: Estimating surface solar irradiance from satellites: Past, present, and future perspectives. Remote Sensing of Environment, 233, 111371, https://doi.org/10.1016/j.rse.2019.111371, 2019.

Kariuki, B. W., and Sato, T.: Interannual and spatial variability of solar radiation energy potential in Kenya using Meteosat satellite. Renewable energy, 116, 88-96, https://doi.org/10.1016/j.renene.2017.09.069, 2018.

Karlsson, K.-G., Anttila, K., Trentmann, J., Stengel, M., Fokke Meirink, J., Devasthale, A., Hanschmann, T., Kothe, S., Jääskeläinen, E., Sedlar, J., Benas, N., van Zadelhoff, G.-J., Schlundt, C., Stein, D., Finkensieper, S., Håkansson, N., and Hollmann, R.: CLARA-A2: the second edition of the CM SAF cloud and radiation data record from 34 years of global AVHRR data. Atmospheric Chemistry and Physics, 17(9), 5809–5828, https://doi.org/10.5194/acp-17-5809-2017, 2017.

Jain, R., Qin, J. and Rajagopal, R.: Data-driven planning of distributed energy resources amidst socio-technical complexities. Nat Energy 2, 17112, https://doi.org/10.1038/nenergy.2017.112, 2017

Jia, A., Liang, S., and Wang, D.: Generating a 2-km, all-sky, hourly land surface temperature product from Advanced Baseline Imager data. Remote Sensing of Environment, 278, 113105, https://doi.org/10.1016/j.rse.2022.113105, 2022a.

Jia, A., Liang, S., Wang, D., Ma, L., Wang, Z., and Xu, S.: Global hourly, 5 km, all-sky land surface temperature data from 2011 to 2021 based on integrating geostationary and polar-orbiting satellite data, Earth Syst. Sci. Data Discuss. [preprint], https://doi.org/10.5194/essd-2022-284, Add to Citavi project by DOI in review, 2022b.

Jia, A., Wang, D., Liang, S., Peng, J., and Yu, Y.: Global daily actual and snow-free blue-sky land surface albedo climatology from 20-year MODIS products. Journal of Geophysical Research: Atmospheres, e2021JD035987, https://doi.org/10.1029/2021JD035987, 2022c.

Letu, H., Nakajima, T. Y., Wang, T., Shang, H., Ma, R., Yang, K., ... and Shi, J.: A new benchmark for surface radiation products over the east Asia–Pacific region retrieved from the Himawari-8/AHI next-generation geostationary satellite. Bulletin of the American Meteorological Society, 103(3), E873-E888, https://doi.org/10.1175/BAMS-D-20-0148.1, 2022.

Li, L., Xin, X., Zhang, H., Yu, J., Liu, Q., Yu, S., and Wen, J.: A method for estimating hourly photosynthetically active radiation (PAR) in China by combining geostationary and polar-orbiting satellite data. Remote Sensing of Environment, 165, 14-26, https://doi.org/10.1016/j.rse.2015.03.034, 2015.

Li, R., Wang, D., and Liang, S.: Comprehensive assessment of five global daily downward shortwave radiation satellite products. Science of Remote Sensing, 4, 100028, https://doi.org/10.1016/j.srs.2021.100028, 2021.

522 Li, R., Wang, D., Liang, S., Jia, A., and Wang, Z.: Estimating global downward shortwave radiation from VIIRS
523   data using a transfer-learning neural network. Remote Sensing of Environment, 274, 112999,
524   https://doi.org/10.1016/j.rse.2022.112999, 2022.

525 Liang, S., Zheng, T., Liu, R., Fang, H., Tsay, S.-C., and Running, S.: Estimation of incident photosynthetically
526   active radiation from moderate resolution imaging spectrometer data. Journal of Geophysical Research,
527   111(D15), 121. https://doi.org/10.1029/2005JD006730, 2006.

528 Liang, S., Wang, D., He, T., and Yu, Y.: Remote sensing of earth's energy budget: Synthesis and review.
529   International Journal of Digital Earth, 12(7), 737-780, https://doi.org/10.1080/17538947.2019.1597189, 2019.

530 Marcos, J., Storkël, O., Marroyo, L., Garcia, M., and Lorenzo, E.: Storage requirements for PV power ramp-rate
531   control. Solar Energy, 99, 28-35, https://doi.org/10.1016/j.solener.2013.10.037, 2014.

532 Palmintier, B., Hale, E., Hansen, T.M., Jones, W., Biagioni, D., Sorensen, H., Wu, H., Hodge, B.M.: IGMS: an
533   integrated ISO-to-appliance scale grid modeling system. IEEE Trans. Smart Grid 8 (3), 1525–1534.
534   https://doi.org/10.1109/ TSG.2016.2604239, 2017.

535 Prince, S. D., & Goward, S. N.: Global primary production: a remote sensing approach, J. Biogeogr., 22(4– 5),
536   815–835, https://doi.org/10.2307/2845983, 1995.

537 Riihelä, A., Key, J. R., Meirink, J. F., Kuipers Munneke, P., Palo, T., and Karlsson, K.-G.: An intercomparison
538   and validation of satellite-based surface radiative energy flux estimates over the Arctic. Journal of Geophysical
539   Research: Atmospheres, 122(9), 4829–4848. https://doi.org/10.1002/2016JD026443, 2017.

540 Rutan, D. A., Kato, S., Doelling, D. R., Rose, F. G., Le Nguyen, T., Caldwell, T. E., and Loeb, N. G.: CERES
541   Synoptic Product: Methodology and Validation of Surface Radiant Flux: CERES1. Journal of Atmospheric
542   and Oceanic Technology, 32(6), 1121–1143. https://doi.org/10.1175/JTECH-D-14-00165.1, 2015.

543 Ryu, Y., Jiang, C., Kobayashi, H., and Detto, M.: MODIS-derived global land products of shortwave radiation
544   and diffuse and total photosynthetically active radiation at 5 km resolution from 2000. Remote Sensing of
545   Environment, 204, 812-825, https://doi.org/10.1016/j.rse.2017.09.021, 2018.

546 Sarr, A., Kebe, C. M. F., Gueye, M., and Ndiaye, A.: Impact of temporal and spatial variability of solar resource
547   on technical sizing of isolated solar installations in Senegal using satellite data. Energy Reports, 7, 753-766,
548   https://doi.org/10.1016/j.egyr.2021.07.064, 2021.

549 Schaaf, C. and Wang, Z.: MCD43A3 MODIS/Terra+Aqua BRDF/Albedo Daily L3 Global - 500m V006, NASA
550   EOSDIS Land Processes DAAC [Data set], https://doi.org/10.5067/MODIS/MCD43A3.006, 2015.

551 Schmetz, J., Pili, P., Tjemkes, S., Just, D., Kerkmann, J., Rota, S., & Ratier, A.: Supplement to An Introduction
552   to Meteosat Second Generation (MSG). American Meteorological Society. https://doi.org/10.1175/bams-83-
553   7-schmetz-2, 2002.

554 Sun, D., Ji, C., Sun, W., Yang, Y., and Wang, H.: Accuracy assessment of three remote sensing shortwave
555   radiation   products   in   the   Arctic: Arctic.   Atmospheric   Research,   212,   296–308.
556   https://doi.org/10.1016/j.atmosres.2018.01.003, 2018.

557 Sweerts, B., Pfenninger, S., Yang, S. et al. Estimation of losses in solar energy production from air pollution in
558   China since 1960 using surface radiation data. Nat Energy 4, 657–663, https://doi.org/10.1038/s41560-019-
559   0412-4, 2019.

560 Tang, W., Yang, K., Qin, J., Li, X., and Niu, X.: A 16-year dataset (2000–2015) of high-resolution (3 h, 10 km)
561   global surface solar radiation, Earth Syst. Sci. Data, 11, 1905–1915, https://doi.org/10.5194/essd-11-1905-
562   2019, 2019.

563 Tapia, M., Heinemann, D., Ballari, D., and Zondervan, E.: Spatio-temporal characterization of long-term solar
564   resource using spatial functional data analysis: Understanding the variability and complementarity of global
565   horizontal   irradiance   in   Ecuador.   Renewable   Energy,   189,   1176-1193,
566   https://doi.org/10.1016/j.renene.2022.03.049, 2022.

567 Van Laake, P. E., and Sanchez-Azofeifa, G. A.: Simplified atmospheric radiative transfer modelling for estimating
568   incident PAR using MODIS atmosphere products. Remote sensing of environment, 91(1), 98-113,
569   https://doi.org/10.1016/j.rse.2004.03.002, 2004.

570 Wang, D., Liang, S., Liu, R., and Zheng, T.: Estimation of daily-integrated PAR from sparse satellite observations:
571   Comparison of temporal scaling methods. International Journal of Remote Sensing, 31(6), 1661-1677,
572   https://doi.org/10.1080/01431160903475407, 2010.

Wang, D., Liang, S., Zhang, Y., Gao, X., Brown, M. G. L., and Jia, A: A New Set of MODIS Land Products (MCD18): Downward Shortwave Radiation and Photosynthetically Active Radiation. Remote Sensing, 12(1), 168. https://doi.org/10.3390/rs12010168, 2020.

Wang, D., Liang, S., Li, R., and Jia, A.: A synergic study on estimating surface downward shortwave radiation from satellite data. Remote Sensing of Environment, 264, 112639, https://doi.org/10.1016/j.rse.2021.112639, 2021.

Wang, D. and Li, R.: A GeoNEX-based 1km hourly land surface downward shortwave radiation (DSR) and photosynthetically active radiation (PAR) product, Zenodo [Data set]. https://doi.org/10.5281/zenodo.7023863, 2022.

Wang, W., Li, S., Hashimoto, H., Takenaka, H., Higuchi, A., Kalluri, S., and Nemani, R.: An introduction to the Geostationary-NASA Earth Exchange (GeoNEX) Products: 1. Top-of-atmosphere reflectance and brightness temperature. Remote Sensing, 12(8), 1267, https://doi.org/10.3390/rs12081267, 2020.

Wei, J., Li, Z., Li, K., Dickerson, R. R., Pinker, R. T., Wang, J., ... and Cribb, M.: Full-coverage mapping and spatiotemporal variations of ground-level ozone (O3) pollution from 2013 to 2020 across China. Remote Sensing of Environment, 270, 112775, https://doi.org/10.1016/j.rse.2021.112775, 2022.

Yan, G., Tong, Y., Yan, K., Mu, X., Chu, Q., Zhou, Y., ... and Zhang, W.: Temporal extrapolation of daily downward shortwave radiation over cloud-free rugged terrains. Part 1: Analysis of topographic effects. IEEE Transactions on Geoscience and Remote Sensing, 56(11), 6375-6394, 10.1109/TGRS.2018.2838143, 2018.

Yang, L., Zhang, X., Liang, S., Yao, Y., Jia, K., and Jia, A.: Estimating surface downward shortwave radiation over china based on the gradient boosting decision tree method. Remote Sensing, 10(2), 185. https://doi.org/10.3390/rs10020185, 2018.

Yip, W. (2019). About geonex. NASA. Retrieved August 8, 2022, from https://www.nasa.gov/geonex/about

Zhang X., Liang S., Zhou G., Wu H., and Zhao X.: Generating global land surface satellite incident shortwave radiation and photosynthetically active radiation products from multiple satellite data. Remote Sensing of Environment, 152, 318–332. https://doi.org/10.1016/j.rse.2014.07.003, 2014.

Zhang, X., Zhao, X., Li, W., Liang, S., Wang, D., Liu, Q., Yao, Y., Jia, K., He, T., Jiang, B., Wei, Y., and Ma, H.: An Operational Approach for Generating the Global Land Surface Downward Shortwave Radiation Product From MODIS Data. IEEE Transactions on Geoscience and Remote Sensing, 57(7), 4636–4650. https://doi.org/10.1109/TGRS.2019.2891945, 2019.

Zhang, Y., He, T., Liang, S., Wang, D., and Yu, Y.: Estimation of all-sky instantaneous surface incident shortwave radiation from Moderate Resolution Imaging Spectroradiometer data using optimization method. Remote sensing of environment, 209, 468-479, https://doi.org/10.1016/j.rse.2018.02.052, 2018.

Zhang, Y., Liang, S., He, T., Wang, D., Yu, Y., and Ma, H.: Estimation of Land Surface Incident Shortwave Radiation From Geostationary Advanced Himawari Imager and Advanced Baseline Imager Observations Using an Optimization Method. IEEE Transactions on Geoscience and Remote Sensing, https://doi.org/10.1109/TGRS.2020.3038829, 2020.